metals

MDPI

Article

Investigation of the Mechanism of Powder Pool Coupled Activating TIG Welding

Yong Huang [1,2,*], Boyang Wang [1], Jianhang Guo [1], Ding Fan [1,2] and Shurong Yu [3]

[1] School of Materials Science and Engineering, Lanzhou University of Technology, Lanzhou 730050, China
[2] State Key Laboratory of Advanced Processing and Recycling of Non-Ferrous Metals, Lanzhou University of Technology, Lanzhou 730050, China
[3] School of Mechanical and Electrical Engineering, Lanzhou University of Technology, Lanzhou 730050, China
* Correspondence: hyorhot@lut.edu.cn

Abstract: As a highly effective welding method, PPCA-TIG (Powder Pool Coupled Activating Flux–Tungsten Inert Gas) welding aims to achieve automated activation of TIG welding through the use of suitable activating fluxes. However, due to the unique transitional behavior of activating elements, the mechanism of PPCA-TIG is a little bit different from common activating TIG welding. In this research, a two-dimensional model is established to investigate the effect of four activating fluxes (TiO_2, SiO_2, MnO_2, CaF_2) on arc morphology and force. A series of welding experiments is performed to study the impact of the different activating elements on the molten pool. The results show that the increase in the penetration of TiO_2 is related to the high arc temperature and great arc force and electromagnetic force in the molten pool. The problem of the softening of 3003 aluminum alloy welded joints is solved. Other activating fluxes are less effective than TiO_2. The addition of calcium fluoride significantly affects penetration. The use of TiO_2, SiO_2 and MnO_2 changes the molten pool viscosity and affects the molten pool oscillation, thus affecting the weld quality.

Keywords: PPCA-TIG welding; numerical simulation; complete penetration; activating fluxes; softened welded joints

Citation: Huang, Y.; Wang, B.; Guo, J.; Fan, D.; Yu, S. Investigation of the Mechanism of Powder Pool Coupled Activating TIG Welding. *Metals* **2023**, *13*, 830. https://doi.org/10.3390/met13050830

Academic Editors: António Bastos Pereira and Aleksander Lisiecki

Received: 21 March 2023
Revised: 6 April 2023
Accepted: 19 April 2023
Published: 23 April 2023

1. Introduction

TIG (Tungsten Inert Gas) welding is employed extensively in modern industry, especially for joining important structures and non-ferrous metals, owing to its stable welding arc, the purity of the molten metal, the beautiful weld surface, and its perfect weld quality. All of these merits are a result of the use of non-consumable tungsten electrodes and inert shielding gases. Regrettably, these same qualities lead to shallow weld penetration and a low deposition rate of filler wire when using this welding process. Tungsten electrodes can only carry a limited amount of current. Particularly for the welding of aluminum, magnesium, and their alloys, alternating-current TIG arcs are usually used to remove the thin dense surface oxide film in the EP (electrode positive) half duration, as well as to prevent the burning of the tungsten electrode in the EN (electrode negative) half duration. This further decreases the weld penetration, and lowers the welding efficiency. To resolve this problem, new variations of the TIG welding method have continuously been researched, developed, and applied in recent decades, including obtaining high efficiency through constricting welding arc [1,2], coupling multi-electrode arcs [3], utilizing high current with forced water-cooling tungsten electrodes [4], and employing a high-frequency pulse current [5].

As a prominent and representative method, activating TIG welding has attracted considerable attention. By introducing activating elements in the form of activating fluxes or activating gases, this method is able to greatly increase weld penetration with low heat input. Activating TIG welding methods can be divided into three categories according to the method of introducing the activating elements; specifically, with activating flux [6–8],

with activating gas [9,10], or with activating flux generated in situ from activating gas [11]. It is expected that the mechanism by which the introduced activating elements dramatically increase weld penetration arises from its effects on the arc and the flow of molten pool metal. The Marangoni convection effect is enhanced by arc contraction or variations in the surface tension temperature gradient of the molten pool, causing inward and downward flow of the metal. This is conducive to improving the weld depth [12–14]. However, there is no consensus on which is the main mechanism for various material combinations of base metals and activating materials (gas or flux).

Introducing activating flux through fluxes is well known, especially for AF-TIG (activating flux) welding. This is the most well-studied and widely used activating TIG welding method. Sometimes the abbreviation A-TIG welding is used to denote the entire activating TIG welding process. In this method, activating fluxes are brushed or sprayed onto the metal surface before common TIG welding is carried out. This method improves the weld penetration of common TIG welding by up to 2–3 times. In addition, by using this method, it is possible to completely penetrate a 12-mm-thick steel plate [15]. Unfortunately, this flux application process is typically manual, hindering the automation of the welding procedure, which has led to novel variations in the activating TIG welding method being proposed. Among these variations, Powder Pool Coupled Activating TIG (PPCA-TIG) welding shows great potential [8]. It employs double layers of shielding gases. The inner and outer double-layer gas channels are narrower than the traditional TIG welding torch. In addition, inert gas is introduced into channels to protect the welding area. Powder particles of the activating flux are sent into the arc space through the outer gas channel, and are finally transferred into the molten pool. The comprehensive effect of the activating fluxes passing through the arc–pool coupling system is a dramatic increase in welding penetration, contributing to high welding efficiency. The introduction of activating elements in PPCA-TIG welding varies considerably from traditional activating TIG welding. In common TIG welding, the base metal melts, forming a molten pool before the activating flux melts. The surface particles then melt into liquid and enter the molten pool. PPCA-TIG welding uses fine powder to send the activating flux particles into the arc space through coaxial powder feeding. The particles are first subjected to the effects of the arc, and melt, evaporate and ionize. The activating elements interact with the molten pool metal in an atomic state on the surface of the molten pool. Then, they are distributed with the flow in the molten pool by means of the internal circulation of the liquid metal.

In the process of PPCA-TIG welding, the periodic changes in the AC arc plasma characteristics are expected to greatly affect the transition behavior of activating flux powders in the arc. This consequently affects the formation and properties of the weld. Successfully researching the characteristics of AC TIG arc plasma in consideration of the structure of a PPCA-TIG welding torch is crucial for achieving industrial application. Cantin and Francis experimentally studied the arc of the AC TIG welding of aluminum, estimating the arc power by means of an equation that included the current recorded using a Hall effect probe and the voltage between the welding torch and the workpiece [16]. Hu et al. measured and analyzed the dynamic variations in electron density near zero current and at current crossing zero for an AC TIG arc with a square wave and a sinusoidal wave based on modern intensified charge-coupled device (ICCD) spectral instrument, and found that there was still a high electron density in the arc during current crossing zero [17]. Yang et al. believed that for the AC TIG arc measured through the ICCD spectral instrument, the electron density demonstrated hysteresis during the current crossing zero stage of different welding waveforms that was related directly to the current and the change rate of the arc input power [18]. However, due to the complex physical and chemical processes in the welding arc, it is difficult to measure many of the properties and dynamic behaviors of the arc using experimental means. Numerical simulation is a fruitful research method for analyzing arc plasma characteristics. Various models of welding arcs, including different numbers of dimensions (2D and 3D) [19–21], shielding gases (argon, helium, nitrogen, and so on) [22,23], electrode tip shapes [24,25], and current waveforms (constant and pulsing

current) [26,27], have been established. Unfortunately, few works in the literature have focused on the simulation of alternating-current arc behaviors, owing to the complexity of alternating-current arcs compared to direct-current arcs. An AC (alternating-current) arc model of plasma arc welding has only been developed by Tashiro et al., with EN ratios of 0.65 and 0.45, which was used to determine the variation in the maxima of plasma temperature, electrode temperature, and the axial velocity of the plasma over time [28]. In addition, beyond the field of welding, several scholars have also carried out simulation research of AC arcs on fault arcs [29,30] and furnace arcs [31,32].

In the present paper, based on actual welding conditions, a two-dimensional transient arc plasma model is established to assess the behaviors of AC arcs of PPCA-TIG welding. In addition, the effects of changing the structure of the welding torch on the arc characteristics are studied. In addition, periodic changes in arc plasma characteristics are analyzed. The effect of using different activating elements on the arc–molten pool system and the reasons for increased penetration of the two activating fluxes were analyzed.

2. Experimental Procedure

A diagram of the experimental platform is shown in Figure 1. Figure 2 shows the PPCA-TIG torch and a diagram representing the coaxial powder feeding and welding process. The torch and powder are made by our research team. The arc length is 3 mm, and other welding parameters are shown in Table 1. The diameter of the tungsten electrode is 2.4 mm. The base metal is a 3003 aluminum alloy plate (200 mm × 100 mm × 8 mm), with a composition as shown in Table 2. The welding parameters were derived from previous studies on PPCA-TIG welding [33]. Four activating fluxes (SiO_2, TiO_2, MnO_2, CaF_2, purchased from Sinopharm Chemical Reagent Co., Ltd., Beijng, China) are used, with a particle size of 1 μm. The supply rate of the powders is 1 g/min. High speed camera, OLYMP US I-Speed 3, purchased from BeiJing Cnrico Technology Co., Ltd., China, is used for recording the behaviors of cathode spots during the process of electrode positive (EP) polarity To keep the arc stable, the camera shoots after 10 s of arc ignition, and the camera is tilted down towards the molten pool; the camera parameters are presented in Table 3. The current waveform is recorded by the data logger, and sent to the computer; the welding signal acquisition system is shown in Figure 3.

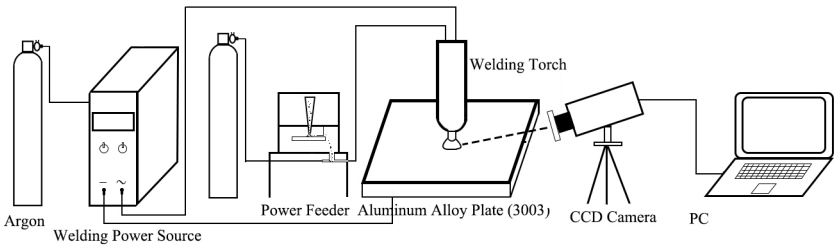

Figure 1. Experimental setup.

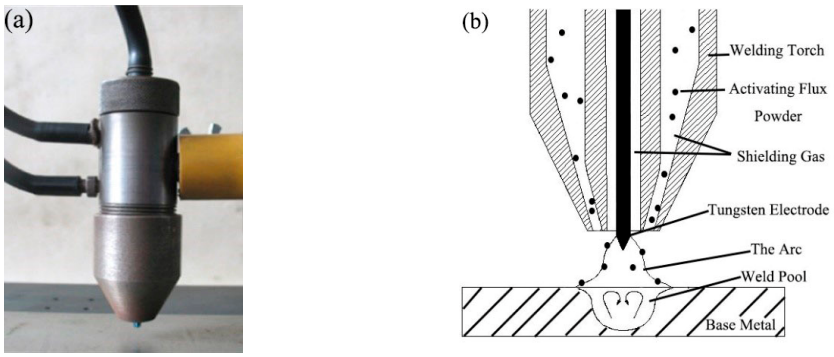

Figure 2. PPCA-TIG welding torch and its nozzle structure (**a**) PPCA-TIG welding torch (**b**) Schematic diagram of the nozzle.

Table 1. Welding parameters.

Current	Speed mm·min^{-1}	Inner Gas Flow L/min	Outer Gas Flow L/min	EP/EN	Shielding Gas
170 A, AC 50 HZ	80	10	12	3/7	Argon (99.99%)

Table 2. Camera parameters.

Camera	FPS	Shutter	Shooting Time (s)	Shooting Distance (cm)	Angle of Depression
OLYMPUS I-Speed 3	40,000	10	4.66	0.3	30°

Table 3. 3003 aluminium alloy compositions (wt%).

Si	Cu	Zn	Mn	Mn	Al
0.6	0.05–0.2	0.1	1.0–1.5	0.7	Margin

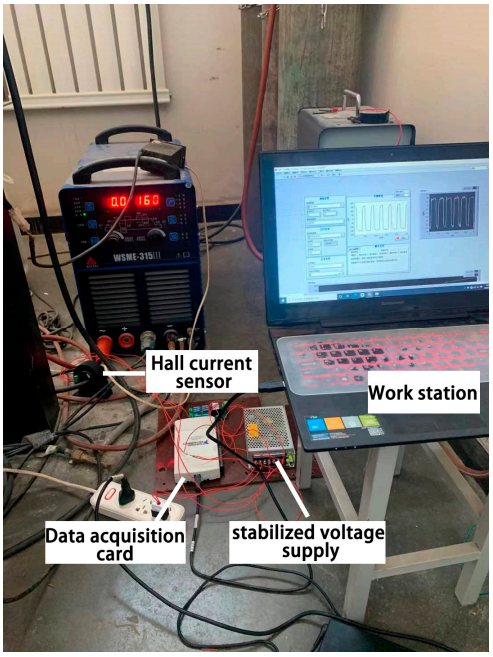

Figure 3. Welding signal acquisition system.

3. Mathematical Model

The calculation domain is shown in Figure 4. Owing to the axisymmetric structures of the welding torch and the arc, a 2D computational domain is employed to improve the calculation efficiency. Figure 4a shows the calculation domain of PPCA-TIG welding, and Figure 4b shows the calculation domain of common TIG welding. In PPCA-TIG welding, the radius of the computational domain is 11 mm. The diameter of the tungsten electrode is 2.4 mm. The tip of the tungsten electrode is hemispherical, with a radius of 1.2 mm. The ABON area represents the tungsten electrode, CDEF is the inner nozzle, GHIJ is the outer nozzle, BC is the inlet of inner gas, FG is the inlet of outer gas, ML is the surface of the molten pool, and ANM is the axis of symmetry. Compared with PPCA-TIG welding, the calculation domain of conventional TIG welding is different only with respect to the torch structure; B′C′ represents the gas channels, and C′D′E′F′ represents the torch nozzle. The mesh size is 0.1 mm and is encrypted near the tungsten.

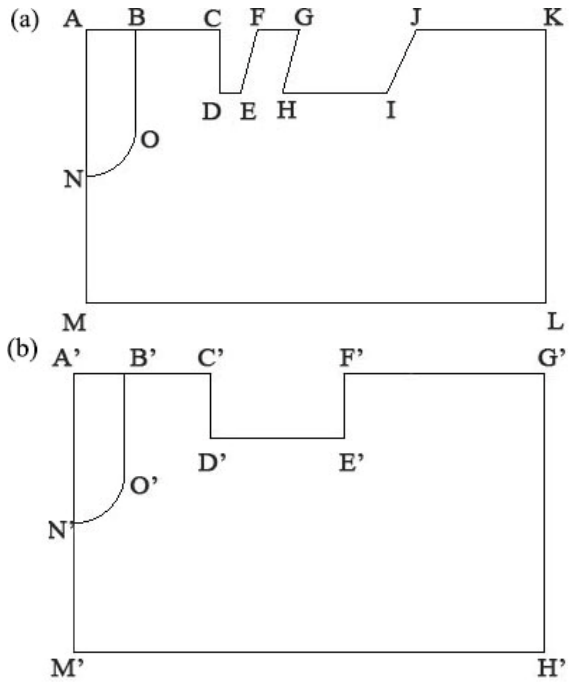

Figure 4. Schematic diagram of the calculation domain (**a**) AC PPCA-TIG welding calculation domain (**b**) Common TIG welding calculation domain.

Arc plasma is commonly supposed to be an elevated gaseous fluid in which the arc current and its self-induced magnetic field interact strongly. A model has been established for AC PPCA-TIG welding arcs. The governing equations are the mass conservation equation, the momentum conservation equation, the energy conservation equation, the current continuity equation, and Ohm's law, as reported by many researchers. Additionally, the arc is affected by electric fields and self-induced magnetic fields.

Table 4 shows the boundary conditions. The current density, which changes periodically with time, is given in the section (AB) of the tungsten electrode. The tungsten electrodes purchase from Beijing BTM Science & Technology Co., Ltd., Beijing, China. The flow velocities of the inner and outer gases are given at BC and FG, respectively, with the velocity-inlet type of boundary condition. In addition, to ensure the current conduction of the arc, an initial temperature of 10,000 K is given before the iterative calculation.

Table 4. Boundary conditions.

Boundary	v/m·s^{-1}	T/K	ϕ/V	A/Wb·m^{-1}
AB	—	2500	$\sigma\frac{\partial\varphi}{\partial n} = j_{given}$	$\frac{\partial A}{\partial n} = 0$
BC	Vgiven1	1000	$\frac{\partial\varphi}{\partial n} = 0$	$\frac{\partial A}{\partial n} = 0$
FG	Vgiven2	1000	$\frac{\partial\varphi}{\partial n} = 0$	$\frac{\partial A}{\partial n} = 0$
JK	$\frac{\partial v}{\partial n} = 0$	1000	$\frac{\partial\varphi}{\partial n} = 0$	$\frac{\partial A}{\partial n} = 0$
KL	$\frac{\partial v}{\partial n} = 0$	1000	$\frac{\partial\varphi}{\partial n} = 0$	$\frac{\partial A}{\partial n} = 0$
LM	—	2500	0	$\frac{\partial A}{\partial n} = 0$
BON	—	coupled	coupled	coupled

As shown in Figure 5, the only function of temperature in the present paper is considered to be the thermal–physical parameters of the plasma. The parameters used for the argon plasma are those reported by Professor A.B. Murphy [34]. For alternating-current plasma, the temperature changes not only with spatial location, but also with time.

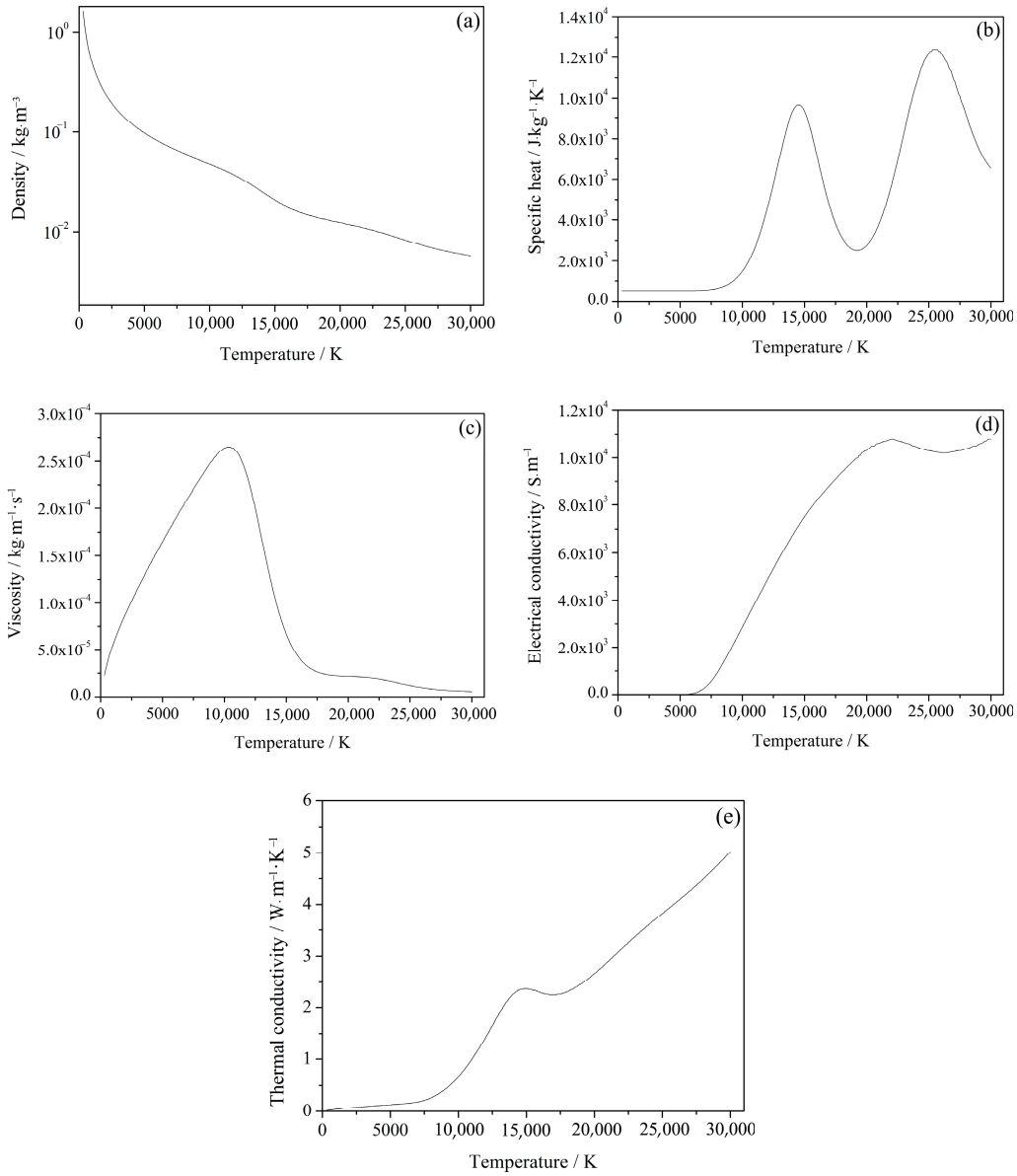

Figure 5. Thermal physical parameters of argon plasma (**a**) density (**b**) specific heat (**c**) viscosity (**d**) electrical conductivity (**e**) thermal conductivity.

The actual arc current waveform measured is square, as shown in Figure 6. The current waveform adopted in the simulation is simplified from the actual measurement results, as shown in Figure 6b. The frequency of the arc current used in the simulation is 50 Hz. The ratio of EN/EP is 1.

Both arc currents are 160 A, and the arc lengths are 3 mm. The shielding gases consist of argon. For the TIG welding, the shielding gas flow rate is 12 L/min. For the PPCA-TIG welding, the inner shielding gas flow rate is 12 L/min and the outer rate is 8 L/min.

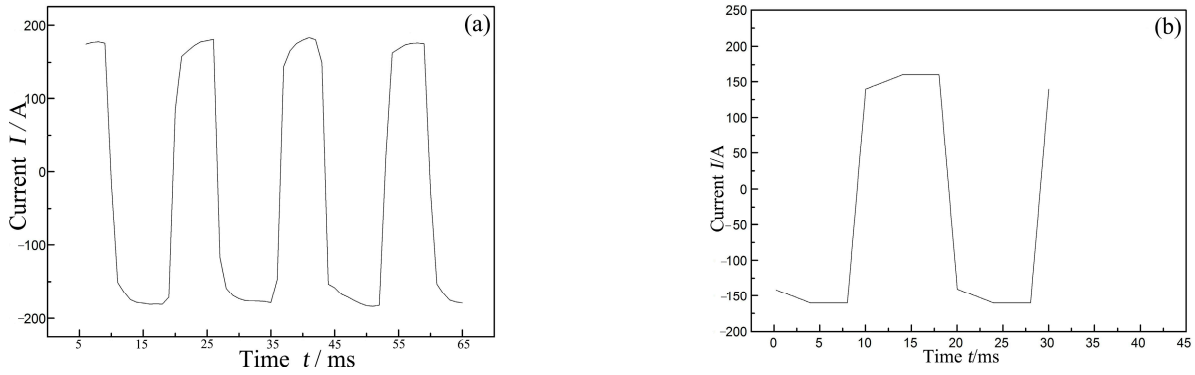

Figure 6. Arc current adopted in simulation (**a**) arc current waveform measured (**b**) fitted current value.

4. Results

Figure 7 shows the weld surface and cross-section morphology with and without activating fluxes. When non-activating flux is used, there are more pores on the weld surface. These pores mostly consist of hydrogen from the atmosphere and the surface of the plates. The hydrogen has no time to escape before the solidification of the molten pool. The aluminum alloy plate is welded completely. However, the weld surface can be seen to form poorly with the use of TiO_2 activating flux. With SiO_2 and MnO_2 activating fluxes, the weld performs badly. The weld surface is covered with black welding slag. However, the former can result in increased penetration, while the latter can reduce it. The contribution of the activating fluxes to penetration depth and width can be seen in the figures. With mixed activating flux, the weld surface performs well, and fish scales appear. Pores are barely visible at the macro scale. Both weld penetration and width are increased. The aluminum alloy plates are welded completely. The ratio of depth and width is shown in Figure 8.

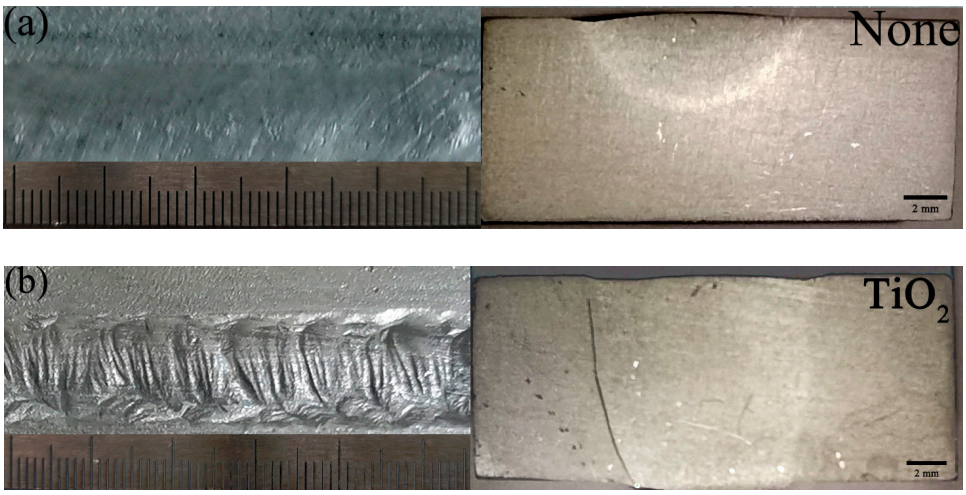

Figure 7. *Cont.*

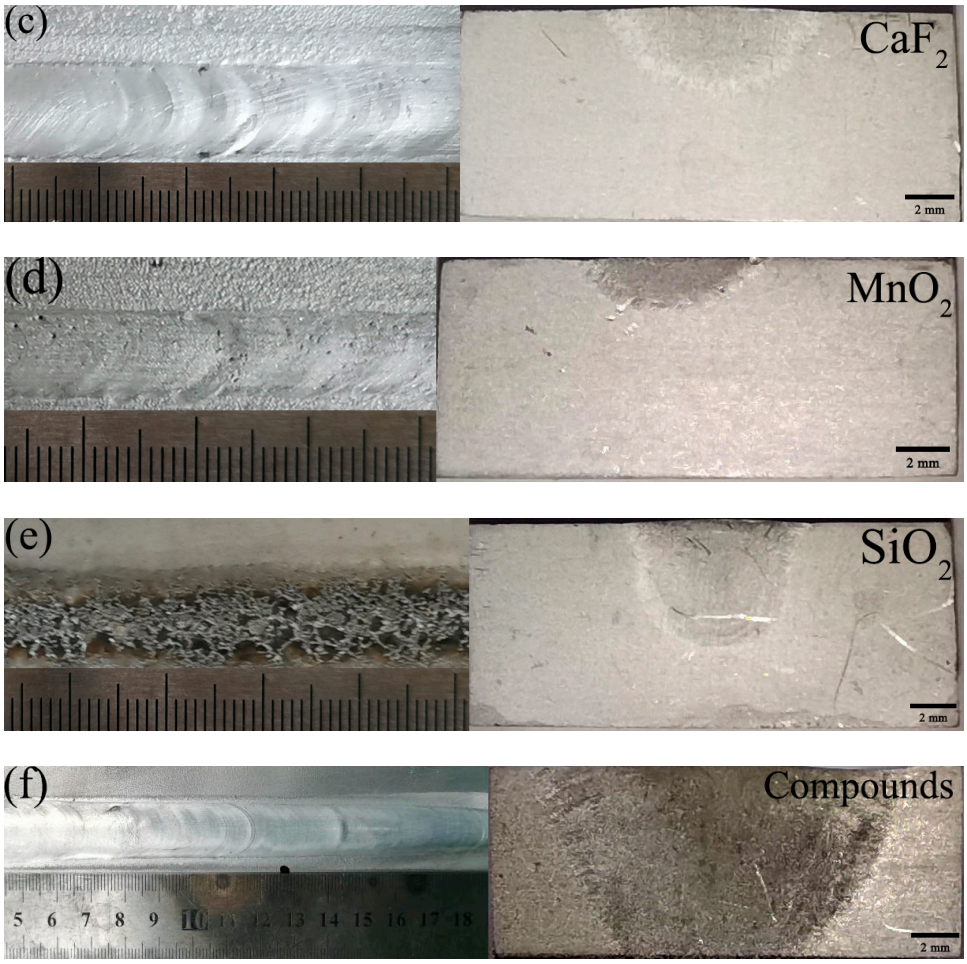

Figure 7. Welded with different activating fluxes (**a**) None; (**b**) TiO_2; (**c**) CaF_2; (**d**) MnO_2; (**e**) SiO_2; (**f**) Compounds.

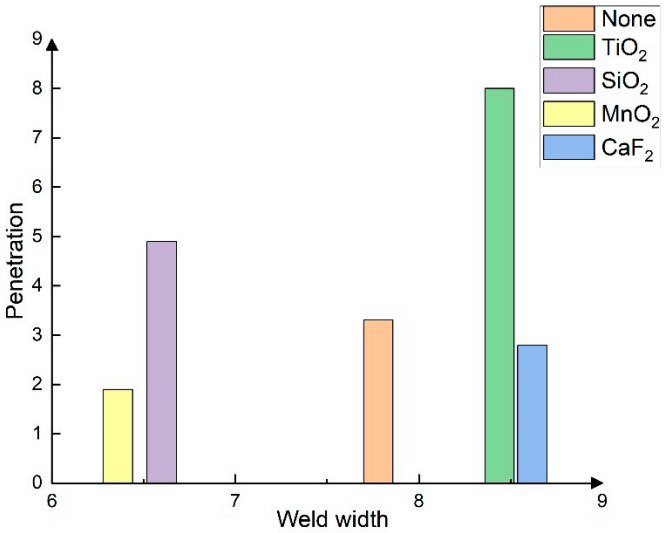

Figure 8. Weld depth to width ratio.

The arc morphology at the maximum current is shown in Figure 9. Compared with non-activating fluxes, the arc shows two different morphologies after using different activating fluxes. One is that the arc spreads outward in a bell-jar shape, and the center is brighter, such as in the case of using TiO_2 and SiO_2. With TiO_2, the arc spreads out more

obviously. The arc stiffness seems to be greater. The other occurs when using CaF_2 and MnO_2, where the arc is very weak and loose in form. The arc stiffness is very poor.

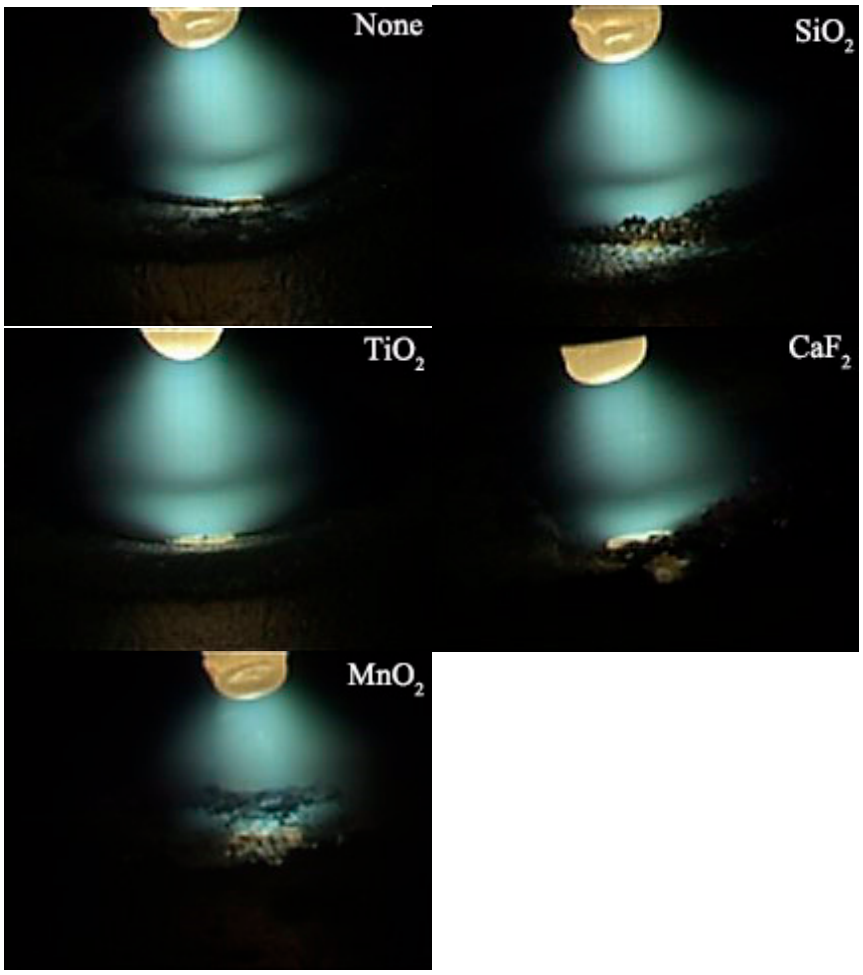

Figure 9. The arc morphology of different activating fluxes.

The liquid metal oscillates at a natural frequency due to arc forces, gravity, and other forces. However, such oscillations on the surface are often difficult to observe directly. Coincidentally, the surface of the SiO_2 and MnO_2 molten pool is covered with a layer of welding slag and oxidation, and the crests and troughs caused by metal flow can be distinguished. Oxide film and welding slag are regarded as references, and the case makes it easy to observe the oscillation of the molten pool. Figure 10a shows the molten pool oscillation on the molten pool surface when using MnO_2, and the amplitude is similar to that of SiO_2. The arrow in the figure represents the molten pool oscillation process. Compared with MnO_2, the amplitude obtained when using TiO_2 as the activating flux was lower, as shown in Figure 10b. With MnO_2, the weld was not fully penetrated and the liquid metal underwent a simple resonant oscillation; a model of this is shown in Figure 10c. The frequency of the molten pool oscillation was statistically analyzed, as shown in Figure 10d. The molten pools of the SiO_2 and MnO_2 activating fluxes oscillate at similar frequencies. The molten pool with the TiO_2 activating flux oscillates at distinctly higher frequencies.

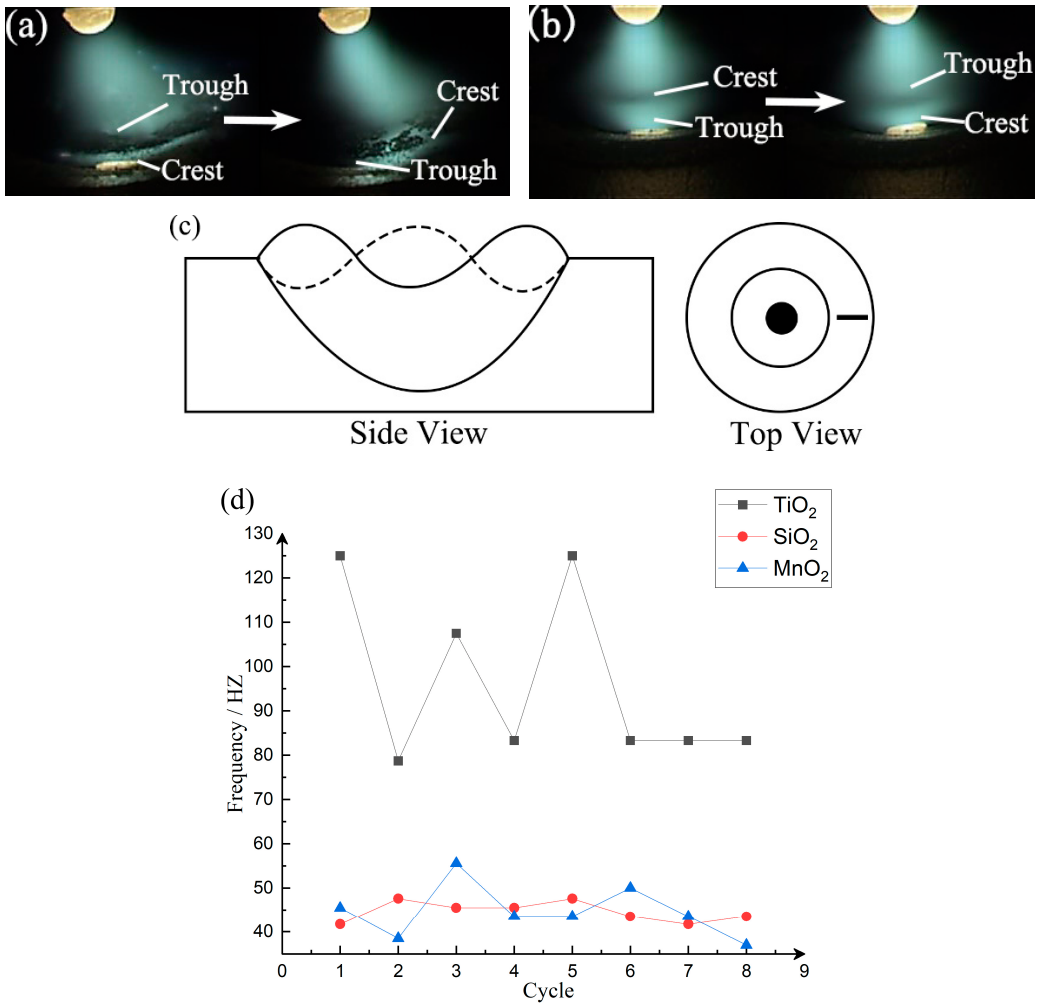

Figure 10. Molten pool fluctuation (**a**) MnO_2 molten pool oscillation; (**b**) TiO_2 molten pool oscillation; (**c**) Oscillation model; (**d**) Oscillation frequency.

Figure 11 shows the tensile mechanical properties of welds produced with different activating fluxes. The welds were sampled according to the GB/T 2652-2008 standard to test their mechanical properties using an AGS-X 300KN (purchased from Shimadzu, Shanghai, China) electronic universal testing machine. In order to measure the tensile strength of the weld, a V-shaped notch of 1 mm was opened at the test weld. The specimens were fractured at the weld except in the case of TiO_2. With the TiO_2, MnO_2, and CaF_2 activating fluxes, the weld strength of the aluminum alloy was higher than the base metal. TiO_2 effectively improves the tensile strength of the aluminum alloy weld, reaching strengths as high as 115% of that of the base metal. However, the weld joint softened when silica activating flux was used. TiO_2 accounted for a large proportion of the mixed activating fluxes, and the tensile fracture morphology was observed using SEM, as shown in Figure 12. When non-activating flux was used, a large number of dimples were produced on the fracture surface. The dimples were large, and there were a lot of pores. With the addition of activating flux compound, the fracture was still ductile. However, the number of pores was significantly reduced, and the dimples were small. Trans-granular dimple fracture characteristics appeared in some areas.

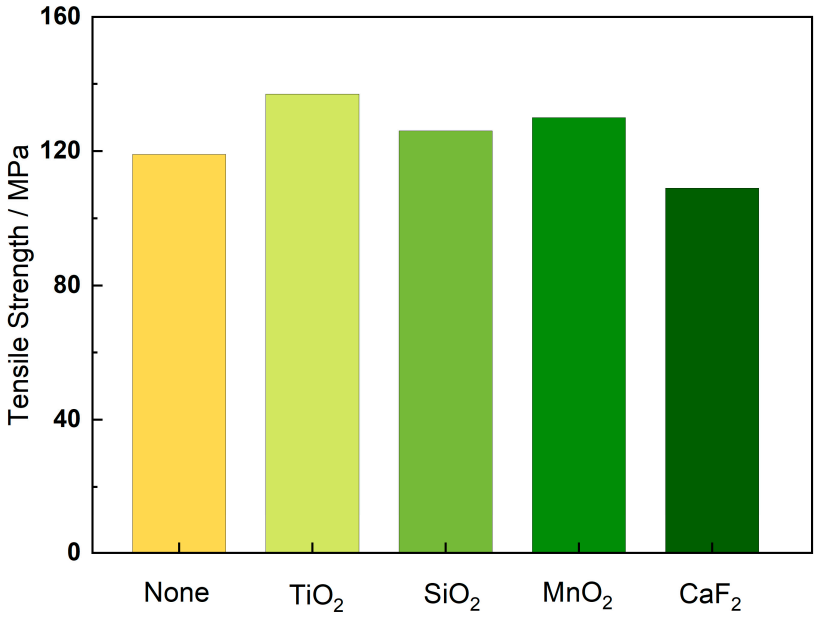

Figure 11. Tensile mechanical properties of the welds.

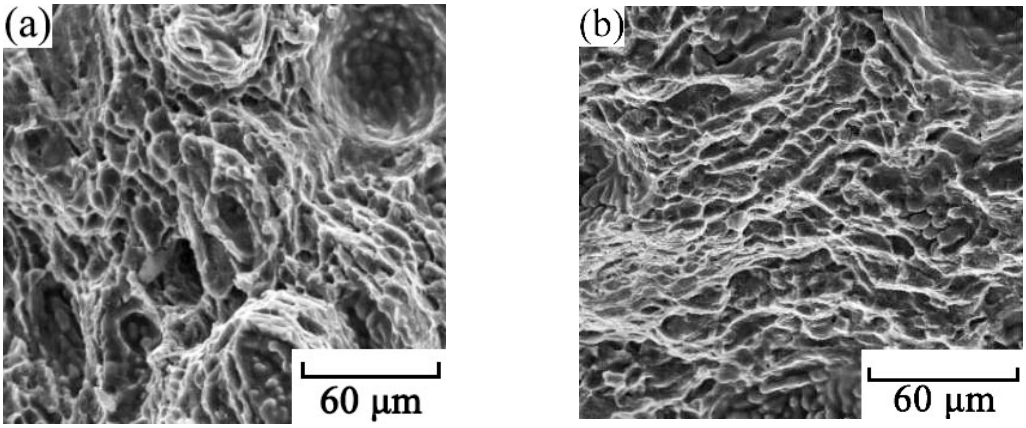

Figure 12. Tensile fracture morphology (**a**) None (**b**) Compounds.

Figure 13 shows a section diagram of the TiO_2 weld. Figure 13a presents the central section of the weld. The grains basically consist of equiaxed grains with good performance and uniform grain sizes. Secondary grain growth occurs in very few regions. Since the TiO_2 weld undergoes full penetration, a sampling point on the right side of the weld is selected. There are slender columnar crystals with a region length of roughly several hundred microns near the fusion line. The grain of the TiO_2 weld is relatively uniform, and the internal area of the weld is basically equiaxed. There are no defects such as pores and cracks in the weld when using TiO_2 as the activating flux. Only a small amount of columnar crystals are present near the weld fusion line. Therefore, the weld produced when using TiO_2 as the activating flux shows good mechanical properties.

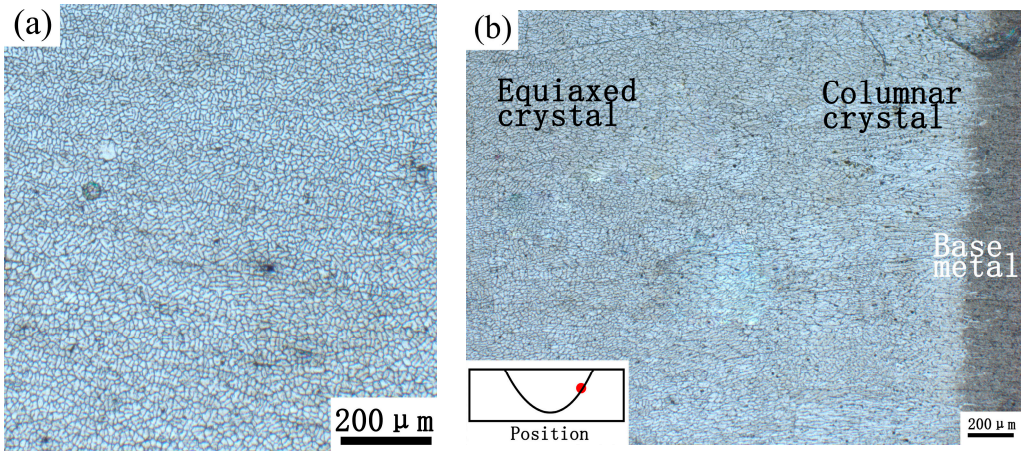

Figure 13. The TiO_2 weld section (**a**) the weld center; (**b**) the weld right side.

Figure 14 shows the weld when using SiO_2 as the activating flux. It can be observed that there are more columnar crystals and almost no fine crystal zone, even at the center of the weld, and there is an equiaxed crystal zone distributed in the area closer to the surface of the weld. In Figure 14b, there are generally coarse columnar crystals near the fusion line, and only a few fine crystals are distributed among the columnar crystals. This indicates that a wide range of columnar crystals are distributed in the SiO_2 weld, and only a small amount of equiaxed crystals are present in the central area of the weld near the surface. Therefore, the mechanical properties of the SiO_2 weld are poor.

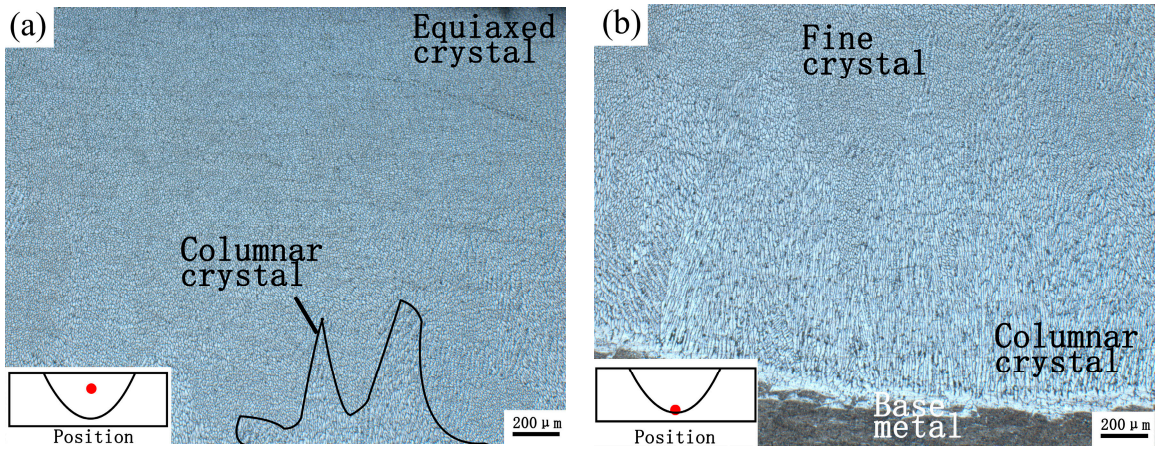

Figure 14. The SiO_2 weld section (**a**) the weld center; (**b**) the weld bottom.

Figure 15 shows the MnO_2 weld. The center and surface of the weld mainly consist of equiaxed crystals, and a small number of fine crystal regions appear below the center of the weld. A row of pores appears in the center of the weld, which are horizontally arranged in the present situation. The size of the pores is relatively uniform, with a diameter of about 30 μm, which indicates that the formation conditions of all pores are similar. In addition, they are generated at the same height in the center of the weld pool. The horizontally arranged pores consist of hydrogen gas that has not been able to escape during the solidification process of the molten pool. A small number of columnar crystal regions exist near the fusion line at the bottom of the weld. The length of the columnar crystal region is about 400 μm. There are a large number of fine crystal regions between the columnar and equiaxed crystals. Therefore, MnO_2 welds have good mechanical properties, but the presence of transversely arranged pores of uniform size in the welds means that the mechanical properties are better than those of SiO_2 welds, but far worse than those of

TiO_2 welds. At the same time, the grain size of the MnO_2 weld is smaller than that of the TiO_2 weld.

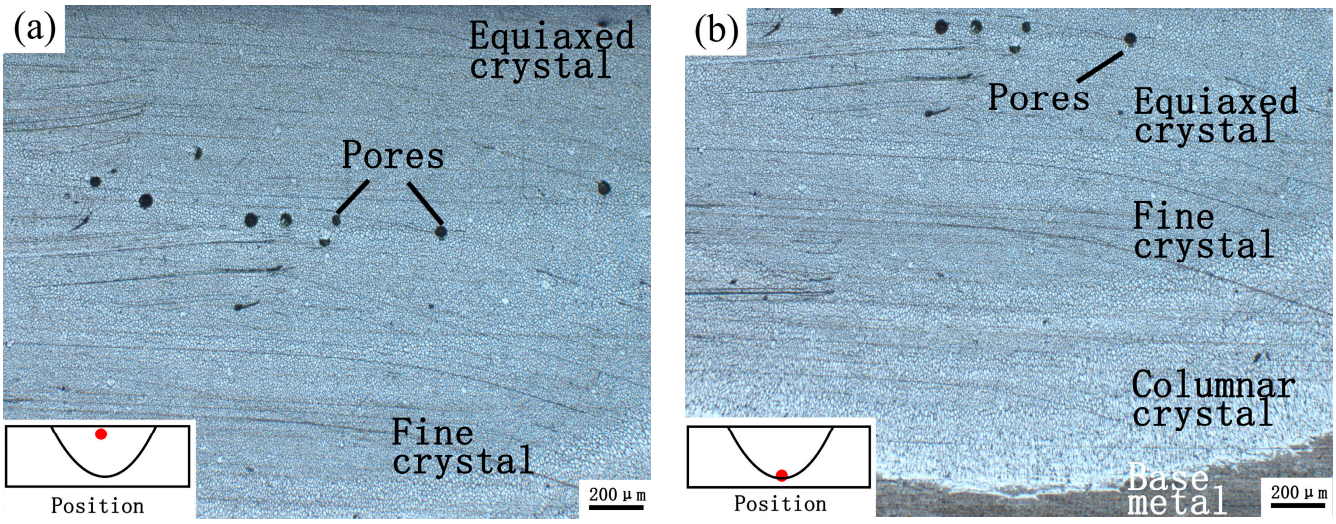

Figure 15. The MnO_2 weld section (**a**) the weld surface; (**b**) the weld bottom.

Figure 16 shows the CaF_2 weld. There are an extremely high number of pores in the CaF_2 weld. These pores are distributed almost throughout the entire weld, but not evenly. The pores range in size from about 300 μm to about ten microns. The porosity is clustered on the surface of the weld. This suggests that the conditions required for the formation of these pores are not consistent. There is a columnar crystal zone about 400 μm length at the bottom of the weld, and grain grows coarsely near the pores. On the one hand, there are a small number of columnar crystals, and the center of the CaF_2 weld is mainly composed of equiaxed crystals, which have good mechanical properties. On the other hand, there are more pores in the weld. The distribution and size of these pores is very uneven, and cracking can easily occur along the pores when subjected to external stress. Therefore, the CaF_2 weld would have very good comprehensive mechanical properties if the problem of porosity in the weld could be solved.

Figure 17 shows the cross-section of the weld of combined activating flux. It has the advantages of all four activating fluxes. As shown in Figure 17a, the equiaxed grain zone in the center of the weld is fine and dense, without pores. However, abnormal grain growth exists in very few areas, which is consistent with the case when using TiO_2 as the activating flux. As shown in Figure 17b, at the surface of the weld, there are equiaxed crystal areas, and a small number of columnar crystals appear near the surface of the weld. The length of this columnar crystal region is about 100–200 μm. As shown in Figure 17c, there are only a few areas near the fusion line on the left side of the weld where columnar crystals are distributed. Most areas are characterized by interactions between fine and columnar crystals. The area of interaction is about 1 mm, and there are a small number of pores at the edge. However, the number of pores is very small, meaning that it will be difficult for them to exert large effects on the weld, such as fracture along the pores.

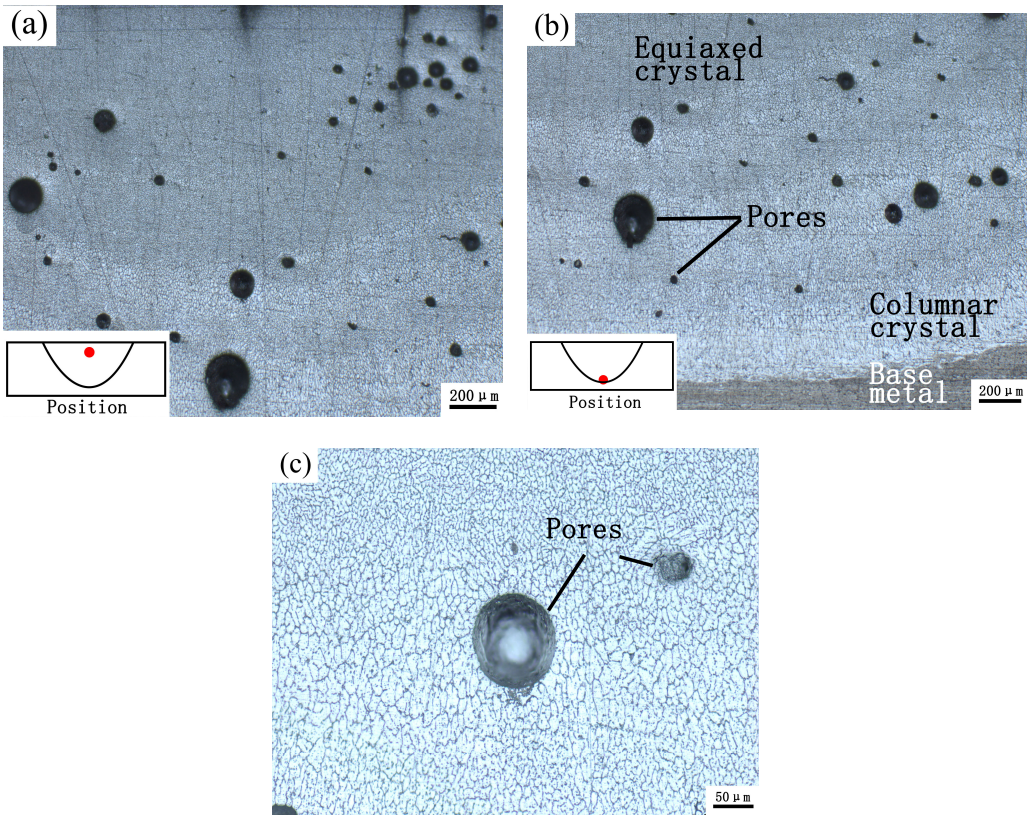

Figure 16. The CaF_2 weld section (**a**) the weld center; (**b**) the weld bottom; (**c**) pores.

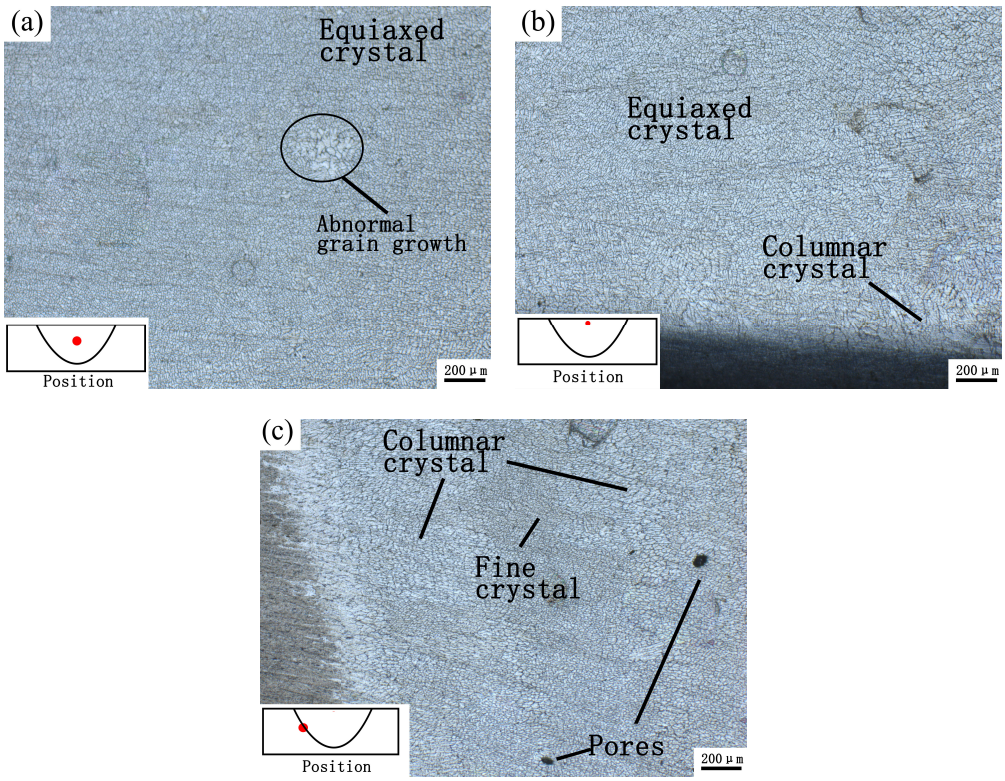

Figure 17. The composed weld section (**a**) the weld center; (**b**) the weld surface; (**c**) the weld left side.

The simulation of the arc temperature field in one cycle is shown in Figure 18. The morphology and temperature varies periodically with the current. The shape and size of the arc are consistent with those observed during the experiment. The simulated arc temperature is also consistent with the temperature distribution measured using the existing spectral method. To some extent, the simulation results are reliable.

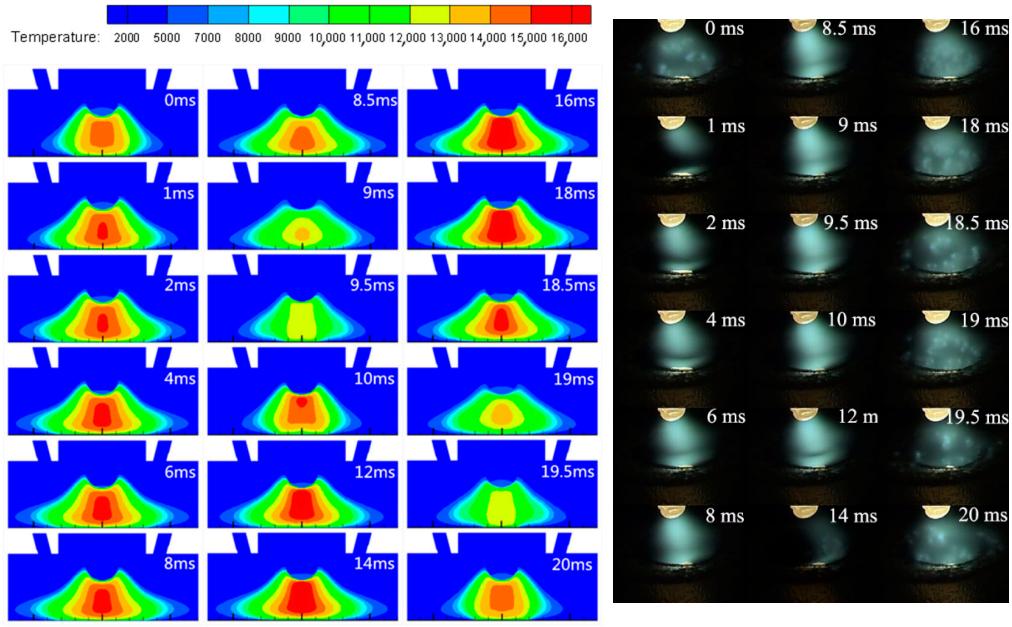

Figure 18. Changes in the arc temperature field during one cycle.

As shown in Figures 19 and 20, the arc morphology and temperature of common TIG welding and both stages of PPCA-TIG welding are compared at the maximum current. The arc maintains a higher temperature in PPCA-TIG welding than in common TIG welding. There is a slight constriction of the arc morphologically. Meanwhile, the energy in the center of the arc is more concentrated and the high-temperature area is larger. Previous results have shown that the arc temperature measured using the spectrum method is higher for PPCA-TIG welding than for common TIG welding.

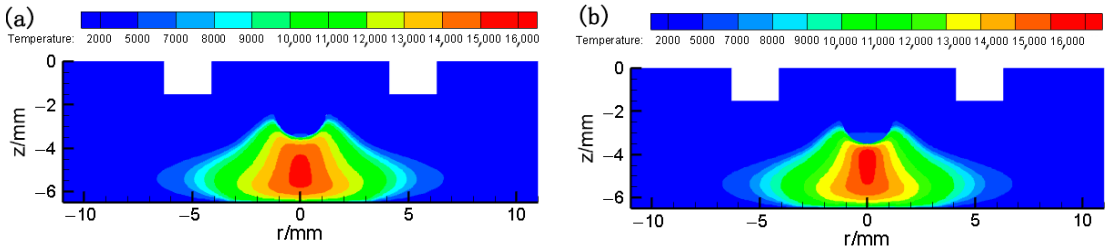

Figure 19. The arc of TIG welding (**a**) EN stage; (**b**) EP stage.

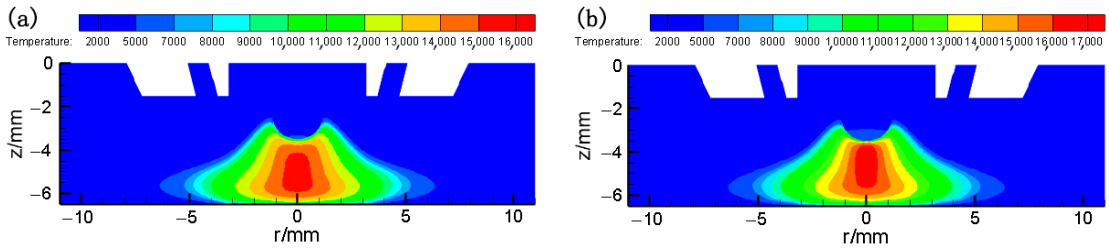

Figure 20. The arc of PPCA-TIG welding (**a**) EN stage; (**b**) EP stage.

5. Discussion

This research presented the impact of using different activating fluxes on the arc and molten pool of aluminum alloy, as well as the changes in the mechanical properties of the weld. Consistent with other papers on activating TIG welding, two activating fluxes, TiO_2 and SiO_2, made a considerable contribution to penetration [35]. TiO_2 activating flux was less effective. Other activating fluxes reduced the penetration. However, in contrast to the general experimental results obtained for activating TIG welding, TiO_2 enabled complete weld penetration. Under the effect of silica, the penetration increased by 2.5 times, which is similar to most experimental results reported for A-TIG. The reasons for this change can be categorized into two aspects: arc and pool.

Firstly, the simulation of PPCA-TIG welding confirmed that the gas channels are more narrow than in ordinary TIG welding, and the gas flow rate is faster. This has a stronger cooling effect on the arc, leading to arc constriction. The temperature of the arc center and the arc force on the surface of the molten pool are higher. With non-activating flux, the shape of the arc shrinks at the macro scale.

The change in arc morphology is also related to the activating elements. The experimental results revealed that the silica causes the arc to shrink slightly, but this may be due to structural changes in the welding torch, not necessarily the effect of the activating element. Under the effect of activating flux TiO_2, the arc expands outward, resulting in better arc stiffness and generating greater arc pressure on the molten pool. The direction of electromagnetic force is directed towards the bottom of the molten pool. The metals in the molten pool move towards the bottom of the molten pool under the action of various forces, contributing to an increase in the liquid metal flow speed, convective intensity, and deep penetration, as shown in Figure 21a. The arc of the other two activating fluxes, MnO_2 and CaF_2, is very weak and of poor arc stiffness. On the one hand, once the active agent has entered the arc, the pyrolysis and ionization processes occur following the spraying of the activating fluxes into the arc. In order to sustain the combustion of the constricted arc, the activating elements weaken the arc, and the arc stiffness decreases. There is also a decrease in arc temperature. On the other hand, a large number of F atoms absorb electrons to form F^-, which leads to obvious constriction of the arc, with poor stiffness and a lower arc temperature. The force of the arc on the surface of the molten pool and the electromagnetic force on the metal have little effect. The driving force of the molten pool metal flow is low, and it moves along the surface of the molten pool. Thus, the molten pool is shallow, as shown in Figure 21b. However, by coating a small amount of CaF_2 on the surface of aluminum alloy welding wire, Li et al. [36] found that the arc was constricted, and the penetration and the ratio of depth to width increased to a certain extent. Therefore, the amount of CaF_2 activating flux added has a significant effect on the welding quality.

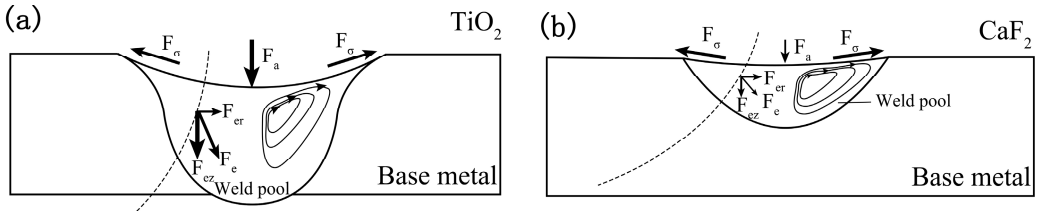

Figure 21. The effect of electromagnetic force and arc force on the molten pool. (**a**) CaF_2 molten pool; (**b**) TiO_2 molten pool.

Secondly, when using TiO_2 activating flux, the frequency of molten pool oscillation was significantly higher than with the other activating fluxes. However, the amplitude of the molten pool was smaller than those of SiO_2 and MnO_2. After the addition of TiO_2, the frequency of the molten pool oscillation was significantly higher than those with addition of the other activating fluxes. However, the amplitude was smaller than those with SiO_2 and MnO_2. This is related to the way in which the activating fluxes enter the molten pool in

PPCA-TIG welding. A diagram of this process is shown in Figure 16. In traditional A-TIG welding, the activating elements enter the molten pool in liquid form, and aluminum atoms infiltrate into the activating molecules, where they interact. In PPCA-TIG welding, the TiO_2 activating flux enters the molten pool surface in the form of Ti atoms through a series of hot processes in the periphery of the arc. The direct interaction is more rapid and intense between the activating elements and the pure metal on the surface of the molten pool, as shown in Figure 22.

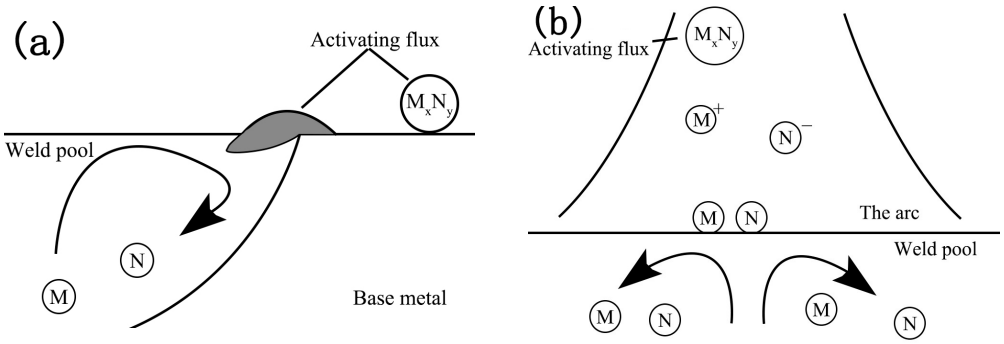

Figure 22. The schematic diagram of activating flux introduction (**a**) A-TIG welding; (**b**) PPCA-TIG welding.

According to the Al-Ti phase diagram [37], aluminum and titanium atoms form the intermetallic compound Al_3Ti at temperatures below 1350 °C. Al_3Ti spreads throughout the molten pool, along with the metal flow in the molten pool, enhancing the viscosity of the liquid metal. According to the results presented in [38], Al_3Ti is distributed in the inter crystal. The second phase of strengthening contributes significantly to the tensile strength of the alloy. For this reason, there was a significant increase in the tensile strength of the aluminum alloy weld with TiO_2 activating flux. This also provides a novel way to achieve aluminum alloy welded joint softening.

On the other hand, with TiO_2 activating flux, the force of the arc acting on the molten pool and the electromagnetic force inside the molten pool are greater. In addition, the trend of the metal flow, resulting in deep penetration in the molten pool, is more obvious. The higher oscillation frequency of TiO_2 in the molten pool changes the distribution of the temperature field in the molten pool. In addition, the newly nucleated grains at the edge of the molten pool remelt under the strong convection of the liquid in the molten pool. Therefore, crystallization at the edge of the molten pool is more difficult, and the thermal cycle time is longer, leading to a deeper melting depth, as shown in Figure 23. Relevant studies have reported that it is difficult to explain the increase in penetration by means of the theory of A-TIG welding pool surface tension gradient change with temperature [39]. Generally speaking, the oscillation frequency of the molten pool is higher under conditions of partial penetration [40,41]; in particular, in the A-TIG welding of aluminum alloy, TiO_2 and SiO_2 have higher oscillation frequencies [42]. However, the viscosity of liquid metal in the molten pool is greatly increased under the effect of SiO_2 and MnO_2 activating flux, resulting in molten pool oscillation at lower frequency and higher amplitude.

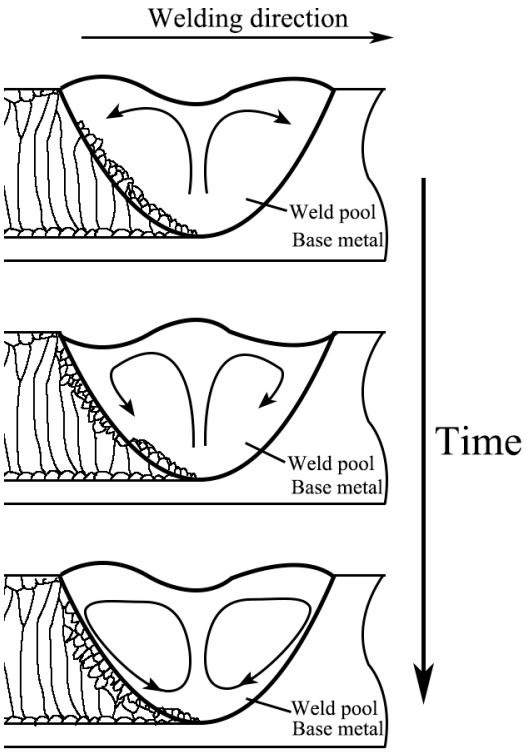

Figure 23. Molten pool oscillation causing grain remelting.

6. Conclusions

In this paper, a PPCA-TIG welding model was established, and the effect on the arc of changing the structure of the PPCA-TIG welding torch was investigated. The effects of activating fluxes on the arc and the molten pool were revealed. The main conclusions are as follows:

1. The PPCA-TIG torch constricts the arc slightly due to the cooling effect of the protective gas.
2. The arc temperature of TiO_2 is higher, and the arc force and electromagnetic force are larger, in the molten pool, which has a significant effect on the metal flow in the molten pool. Therefore, the penetration is increased. In addition, the mechanical properties are better.
3. Under the effect of TiO_2, SiO_2 and MnO_2, the viscosity of the molten pool changes significantly. The molten pool oscillates more frequently with TiO_2, and at a larger amplitude with SiO_2 and MnO_2.
4. The use of single-component activating flux made it possible to achieve good mechanical properties in the weld, except for when using SiO_2. This is mainly determined by the grains in the weld. The TiO_2, MnO_2, and CaF_2 weld are mainly composed of equiaxed crystals, with a small amount of columnar crystals near the fusion line. A large number of columnar crystals grow from the fusion line in the weld when using SiO_2, resulting in poor mechanical properties.

Author Contributions: Y.H.: conceptualization, methodology, data curation, formal analysis and investigation, resources; B.W.: experiment and test, formal analysis and investigation, writing—original draft preparation; J.G.: data curation, experiment and test; D.F.: conceptualization, methodology, supervision; S.Y.: conceptualization, methodology. All authors have read and agreed to the published version of the manuscript.

Funding: This work was funded by the National Natural Science Foundation of China (Grant No. 51965036).

Data Availability Statement: The data presented in this study are available on request from the corresponding author.

Conflicts of Interest: All authors read and approved the final manuscript and declare no financial or competing interest.

References

1. Tian, Q.L.; Yang, X.M.; Chen, L.; Zhang, Y.; Lei, Y.C.; Yan, J.C. Arc behaviour and weld formation in gas focusing plasma arc welding. *Sci. Technol. Weld. Join.* **2020**, *25*, 329–335.
2. Sahoo, A.; Tripathy, S. Development in plasma arc welding process: A review. *Mater. Today Proc.* **2021**, *41*, 363–368. [CrossRef]
3. Ogino, Y.; Hirata, Y.; Nomura, K. Numerical analysis of the heat source characteristics of a two-electrode TIG arc. *J. Phys. D Appl. Phys.* **2011**, *44*, 215202. [CrossRef]
4. Liu, Z.; Chen, S.; Liu, S.; Luo, Z.; Yuan, J. Keyhole dynamic thermal behaviour in K-TIG welding process. *Int. J. Heat. Mass. Transf.* **2018**, *123*, 54–66. [CrossRef]
5. Li, W.; Lv, G.; Wang, Q.; Huang, S. Arc characteristics and weld bead microstructure of Ti-6Al-4V titanium alloy in ultra-high frequency pulse Gas Tungsten Arc welding (UHFP-GTAW) process. *Mater. Sci.* **2020**, *26*, 426–431. [CrossRef]
6. Cai, Y.; Luo, Z.; Zeng, Y. Influence of deep cryogenic treatment on the microstructure and properties of AISI304 austenitic stainless steel A-TIG weld. *Sci. Technol. Weld. Join.* **2017**, *22*, 236–243. [CrossRef]
7. Fan, D.; Huang, Y. Study on activating TIG welding for aluminium alloys. *Weld. World* **2005**, *49*, 22–25.
8. Huang, Y.; Zhao, W.Q.; Zhang, L.Y. Powder pool coupled activating TIG welding method. *Mater. Rep. B* **2017**, *31*, 70–74.
9. Fujii, H.; Sato, T.; Lu, S.; Nogi, K. Development of an advanced A-TIG (AA-TIG) welding method by control of Marangoni convection. *Mater. Sci. Eng. A* **2008**, *495*, 296–303. [CrossRef]
10. Huang, Y.; Liu, R.; Fan, D.; Kang, Z.; Hao, Y.; Qu, H. Gas pool coupled activating TIG welding method. *Trans. China Weld. Inst.* **2012**, *33*, 13–16.
11. Mizutani, M.; Katayama, S. TIG weld penetration improvement by laser-activated process with oxygen. *Weld. World* **2012**, *56*, 21–29. [CrossRef]
12. Howse, D.S.; Lucas, W. Investigation into arc constriction by active fluxes for tungsten inert gas welding. *Sci. Technol. Weld. Join.* **2000**, *5*, 189–193. [CrossRef]
13. Tanaka, M.; Shimizu, T.; Terasaki, T.; Ushio, M.; Koshiishi, F.; Yang, C.-L. Effects of activating flux on arc phenomena in gas tungsten arc welding. *Sci. Technol. Weld. Join.* **2000**, *5*, 397–402. [CrossRef]
14. Heiple, C.R.; Roper, J.R.; Stagner, R.T.; Aden, R.J. Surface active element effects on the shape of GTA, laser and electron beam welds. *Weld. J.* **1983**, *62*, 72–77.
15. Fan, D.; Zhang, R.; Gu, Y.; Ushio, M. Effect of Flux on A-TIG Welding of mild steels. *Trans. JWRI* **2001**, *30*, 35–40.
16. Cantin, G.M.D.; Francis, J.A. Arc power and efficiency in gas tungsten arc welding of aluminium. *Sci. Technol. Weld. Join.* **2005**, *10*, 200–210. [CrossRef]
17. Hu, K.P.; Song, Y.L.; Xia, Y.; Chen, Z.X. Current zero period process and its characteristics of AC TIG arc. *Trans. China Weld. Inst.* **2006**, *27*, 29–33.
18. Yang, X.H.; Song, Y.L.; Hu, K.P. Characteristic of time-energy distribution at current-zero period on AC TIG welding arc. *Trans. China Weld. Inst.* **2009**, *30*, 21–24.
19. Hsu, K.C.; Etemadi, K.; Pfender, E. Study of the free burning high intensity argon arc. *J. Appl. Phys.* **1983**, *54*, 1293–1301. [CrossRef]
20. Xu, G.; Hu, J.; Tsai, H.L. Three-dimensional modeling of the plasma arc in arc welding. *J. Appl. Phys.* **2008**, *104*, 103301. [CrossRef]
21. Wang, X.-X.; Ding, F.; Huang, J.-K.; Huang, Y. Numerical simulation of coupled arc in double electrode tungsten inert gas welding. *Acta Phys. Sin.* **2013**, *62*, 228101. [CrossRef]
22. Lowke, J.J.; Morrow, R.; Haidar, J.; Murphy, A.B. Prediction of gas tungsten arc welding properties in mixtures of argon and hydrogen. *IEEE Trans. Plasma Sci.* **1997**, *25*, 925–930. [CrossRef]
23. Lei, Y.C.; Li, C.H.; Yu, W.; Cheng, X. Numerical analysis of N2-Ar protecting tungsten inert gas welding arc. *Trans. China Weld. Inst.* **2006**, *27*, 25–28.
24. Ushio, M.; Matsuda, F. Mathematical modelling of heat transfer of welding arc. *Trans. JWRI* **1982**, *11*, 7–15.
25. Lee, S.Y.; Na, S.J. A numerical analysis of a stationary gas tungsten welding arc considering various electrode angles. *Weld. J.* **1996**, *75*, 269–279.
26. Murphy, A.B.; Tanaka, M.; Yamamoto, K.; Tashiro, S.; Sato, T.; Lowke, J.J. Modelling of thermal plasmas for arc welding: The role of the shielding gas properties and of metal vapour. *J. Phys. D Appl. Phys.* **2009**, *42*, 194006. [CrossRef]
27. Shi, Y.; Guo, C.B.; Huang, J.K.; Fan, D. Numerical simulation of pulsed current tungesten inert gas (TIG) welding arc. *Acta Phys. Sin.* **2011**, *60*, 048102.
28. Tashiro, S.; Miyata, M.; Tanaka, M. Numerical simulation of AC plasma arc welding. *J. Jpn. Weld. Soc.* **2009**, *27*, 1–3. [CrossRef]
29. Rong, M.Z.; Li, M.; Wu, Y. 3-D MHD modeling of internal fault arc in a closed container. *IEEE Trans. Power Deliv.* **2017**, *32*, 1220–1227. [CrossRef]
30. Chen, Z.; Zou, X.B.; Li, H.D. Numerical simulation of acoustic wave generated by the AC arc. *IEEE Trans. Plasma Sci.* **2019**, *47*, 4136–4141. [CrossRef]

31. Moghadam, M.M.; Seyedein, S.H.; Aboutalebi, M.R. Fluid flow and heat transfer modeling of AC arc in ferrosilicon submerged arc furnace. *J. Iron Steel Res. Int.* **2010**, *17*, 14–18. [CrossRef]
32. Dong, Q.P.; Zhang, J.M. Simulation of fluid flow and heat transfer in plasma arc region of AC electric arc furnace. *CFD Model. Simul. Mater. Process.* **2016**, *2*, 35–42.
33. Huang, Y.; Li, Q.; Xue, X.; Xu, H.; Huang, J.; Fan, D. Electrostatic probe analysis of SiO_2 activating flux powders transition behavior in Powder Pool Coupled Activating TIG alternating current arc plasma for aluminum alloy. *J. Manuf. Process.* **2022**, *84*, 600–609. [CrossRef]
34. Murphy, A.; Arundell, C.J. Transport coefficients of argon, nitrogen, oxygen, argon-nitrogen, and argon-oxygen plasma. *Plasma Chem. Plasma Process.* **1994**, *14*, 451–490. [CrossRef]
35. Yan, K.; Yang, G.; Zhao, Y. Analysis of arc spectrum in A-TIG welding of aluminum alloy. *Trans. China Weld. Inst.* **2012**, *33*, 73–76.
36. Li, H.; Li, Z.-X.; Cong, X. Effect of fluoride lubricant coating on porosity resistance of aluminum alloy wire. *Chin. J. Nonferrous Met.* **2022**, *32*, 1373–1382.
37. Liu, Z.; Rakita, M.; Wang, X.; Xu, W.; Han, Q. In situ formed Al_3Ti particles in Al alloy matrix and their effects on the microstructure and mechanical properties of 7075 alloy. *J. Mater. Res.* **2014**, *29*, 1354–1361. [CrossRef]
38. Lei, Y.C.; Li, X.; Cui, J. Effect of Ti and Zr on in-situ welding properties of cold metal transition aluminum alloy. *Chin. J. Nonferrous Metals* **2015**, *25*, 2057–2065.
39. Huang, Y. Study on Active TIG welding of aluminum alloy and its mechanism of increasing penetration, Lanzhou University of Technology. *J. Mech. Eng.* **2007**, 45–49.
40. Aendenroomer, A.J.R.; Den Ouden, G. Weld Pool Oscillation as a Tool for Penetration Sensing during Pulsed GTA Welding. *Mater. Sci.* **1985**, *77*, 181–187.
41. Maruo, H.; Hirata, Y. Natural frequency and oscillation modes of weld pools. 1st Report: Weld pool oscillation in full penetration welding of thin plate. *Weld. Int.* **1993**, *7*, 614–619. [CrossRef]
42. Li, C.K.; Dai, Y.; Wang, J.X. Effect of flux on surface tension of liquid metal in welding pool. *J. Jilin Univ. (Eng. Technol. Ed.)* **2022**. [CrossRef]